RSC Advances

PAPER

View Article Online
View Journal | View Issue

Cite this: *RSC Adv.*, 2025, **15**, 44797

Lanthanide-based coordination polymers: a fluorometric Frontier in explosive sensing

Samika Anand,[a] Abhishek Kumar,[cd] Kalathiparambil Rajendra Pai Sunajadevi, *[a] Channabasaveshwar V. Yelamaggad*[bcd] and Kaustava Bhattacharyya [ef]

Received 18th April 2025
Accepted 30th October 2025

DOI: 10.1039/d5ra02731d

rsc.li/rsc-advances

In the pursuit of public safety, environmental protection, and counter-terrorism, significant advancements have been made in explosive detection techniques. However, challenges such as limited sensitivity, poor selectivity, and high operational costs remain, particularly for trace-level detection. In this study, we present a simple and scalable synthesis of lanthanide-based coordination polymers (Ln-COPs), denoted as Ho(DAB) and Tb(DAB), formed through the coordination of Ho(III) and Tb(III) ions, respectively, with the organic linker 3,3′-diaminobenzidine (DAB). Spectroscopic and electron microscopic analyses confirm their two-dimensional planar structure, resulting from the self-assembly of infinitely long polymeric strands. These luminescent Ln-COPs demonstrate exceptional performance as sensors for detecting both nitroaromatic and non-nitroaromatic explosives *via* fluorescence quenching. Notably, Tb(DAB) exhibits a remarkable limit of detection of 7.7 μM for TNP. Furthermore, mechanistic insights into the quenching process are explored. These results underscore the sensitivity and practical applicability of Ln-COPs in advanced explosive detection systems.

Introduction

High-energy materials (HEMs), particularly explosives, are crucial to various sectors, such as mining, defense, and construction. They provide essential energy for blasting in mines, demolition in construction, and strategic applications in the military. Despite these benefits, the use of explosives is associated with considerable risks, from accidental detonations to environmental damages. Furthermore, the easy access and the potential for misuse of explosives in acts of terrorism and criminal activities pose a constant threat to civilian safety, making the development of reliable detection systems imperative.[1,2]

Explosives can be broadly divided into two categories: nitroaromatic and non-nitroaromatic compounds. Nitroaromatic explosives, such as 4-nitrophenol (PNP); 2,4,6-trinitrophenol (TNP), commonly known as picric acid; and 2,4,6-trinitrotoluene (TNT), are based on aromatic rings with nitro groups. These compounds are typically stable under normal conditions but can become highly reactive in the presence of specific triggers, making them valuable yet dangerous. Non-nitroaromatic explosives, such as 1,3,5-trinitroperhydro-1,3,5-triazine (RDX), pentaerythritol tetranitrate (PETN), and hexanitrohexaazaisowurtzitane (CL-20), lack nitro groups but are equally hazardous. These compounds are generally more sensitive to physical stimuli, *viz.*, heat, friction, and pressure, and they pose even greater challenges for detection due to their lack of a predictable aromatic signature. While nitroaromatics typically exhibit strong electron-accepting behavior that makes them relatively easy to detect, non-nitroaromatic explosives often lack this property, making them difficult to identify using standard detection techniques.[3–5]

The widespread deployment and use of HEMs, including both military and civilian explosives, have led to the accumulation of explosive residues across diverse environments. Explosive residues, though present in trace amounts, pose significant risks due to their potential to trigger unintentional explosions, environmental contamination, and health hazards, including skin irritation, respiratory issues, and potential carcinogenic effects. These risks are amplified in densely populated areas, where even a small amount of explosive material can lead to catastrophic consequences.[6] In such public spaces, detection systems capable of identifying trace explosive residues are essential to ensure civilian safety and support rapid, proactive response measures. Therefore, a detection system that can accurately identify explosives, even in trace quantities, is vital.

Existing detection methods for detecting explosives include energy-dispersive X-ray diffraction,[7] plasma desorption mass spectrometry,[8] surface-enhanced Raman spectroscopy,[9] ion

[a]*Department of Chemistry, Christ University, Bangalore-560029, Karnataka, India. E-mail: sunajadevi.kr@christuniversity.in; yelamaggad@cens.res.in*

[b]*SJB Institute of Technology, Health & Education City, Kengeri, Bengaluru–560060, Karnataka, India*

[c]*Department of Chemistry, Manipal Institute of Technology, Manipal Academy of Higher Education, Manipal 576104, Karnataka, India*

[d]*Centre for Nano and Soft Matter Sciences (CeNS), Arkavathi, Survey No. 7, Shivanapura, Dasanapura Hobli, Bengaluru 562162, Karnataka, India*

[e]*Chemistry Division, Bhabha Atomic Research Centre, Mumbai, 400085, India*

[f]*Homi Bhabha National Institute, Anushaktinagar, Mumbai, 400094, India*

mobility spectrometry,[10] chromatography,[11] and electrochemical methods.[12] While these methods offer high sensitivity and accuracy, they often require expensive, bulky equipment, complex sample preparation, and frequent calibrations by skilled personnel, thereby limiting their applicability in real-world, field-based scenarios. Moreover, these methods are susceptible to interference from contaminants and other environmental factors, which can compromise data reliability, often resulting in false readings or false negatives, especially for low-concentration explosives in complex sample matrices.

In contrast, fluorescence-based sensing offers a practical and efficient alternative for field applications. This method leverages the unique luminescent responses that occur when explosive molecules interact with specific sensor materials, providing a rapid, sensitive, and cost-effective approach. Fluorescence sensors are highly portable, require minimal calibration, and produce real-time responses to trace amounts of explosives. Additionally, their simplicity in design and operation makes them ideal for wide-scale deployment in diverse environments, making them particularly suitable for safeguarding public spaces where fast, accurate detection is essential.[13–15] Fluorescent sensors rely on optical response, exhibiting variations in fluorescence intensity, wavelength shifts, or even color change upon interaction with explosive molecules. This interaction often results from electron transfer or quenching processes, which disrupt the fluorescence response of the sensing material, providing a clear, real-time signal that explosives are present.

Various fluorophores, such as metal–organic frameworks (MOFs), covalent organic frameworks (COFs), quantum dots, molecular sensors, and polymer nanocomposites, have been designed to detect nitroaromatic compounds, particularly TNP.[16–20] This detection primarily occurs through fluorescence quenching, driven by charge-transfer processes between the electron-deficient nitroaromatics and the electron-rich fluorophores. Lanthanide-based coordination polymers (Ln-COPs) remain largely underexplored in this context.

Ln-COPs represent a versatile class of functional materials distinguished by their hybrid structure of lanthanide metal nodes coordinated with organic ligands. These organic linkers, typically carboxylates, phosphonates, pyridines, or imidazoles, act as connectors between the metal nodes, forming well-ordered, porous frameworks. The coordination bonds between metal ions and organic ligands provide structural integrity, while the organic ligands add functionality and enable tuning of the material's properties.[21–23] The structural design of Ln-COPs starts with the formation of one-dimensional (1D) chains through metal–ligand coordination bonds. These chains can then undergo self-assembly *via* secondary interactions, such as hydrogen bonding, π–π stacking, dipole–dipole, and van der Waals forces, leading to the creation of two-dimensional (2D) sheets or three-dimensional (3D) frameworks.[23–25] The resulting structural diversity is influenced by the choice of metal ions and ligands, which allows extensive customization to target specific applications. This adaptability has made Ln-COPs ideal for applications that benefit from large surface areas, robust porosity, enhanced adsorption properties, and unique optical and magnetic characteristics.

The combination of the distinct photophysical properties of lanthanides, such as high fluorescence, stability under environmental variations, and sharp emission peaks, with the structural flexibility of organic frameworks, positions Ln-COPs as advanced materials for sensing HEMs.[25] In particular, Ln-COPs hold significant promise as fluorometric sensors for explosives, where their unique luminescent properties, long lifetimes, high sensitivity to changes in their local environment, real-time response, and selectivity can be finely tuned for trace-level detection of both nitroaromatic and non-nitroaromatic explosives.[26,27] Recent studies have shown that COPs with the ability to form continuous 2D layers can function as highly selective and sensitive fluorescence chemosensors for HEMs.[28] However, to be effectively used in explosive detection devices, these COPs must exhibit high resistance to heat, moisture and air; be cost-effective; and be scalable for industrial applications. This presents a significant challenge in designing and developing multifunctional COPs that meet these stringent criteria.

Building on our prior work in synthesizing multifunctional COPs,[28–31] herein, we report a simplistic synthesis and characterization of two Ln-COPs abbreviated as Ho(DAB) and Tb(DAB). The synthesized Ln-COPs demonstrate remarkable fluorescence quenching capabilities with high sensitivity for both nitroaromatic and non-nitroaromatic explosives and impressive detection limits. The choice of Ho(III) and Tb(III) ions in the synthesis of Ln-COPs is guided by their optical and structural properties, which make them ideal candidates for luminescent sensing applications.

Materials and methods

Materials

All the chemicals procured were utilized without modification. Analytical-grade solvents obtained from Merck were dried using customary protocols before use. 3,3′-Diaminobenzidine (DAB) was obtained from TCI Chemicals, whereas holmium(III) acetate hydrate ($Ho(OAc)_3 \cdot H_2O$) and terbium(III) acetate hydrate ($Tb(OAc)_3 \cdot H_2O$) were obtained from Sigma-Aldrich.

Preparation of lanthanide-based COPs

The lanthanide-based COPs were synthesized using a straightforward approach under ambient conditions (Fig. 1).[29–31] An aqueous solution of metal acetate, specifically $Ho(OAc)_3 \square H_2O$

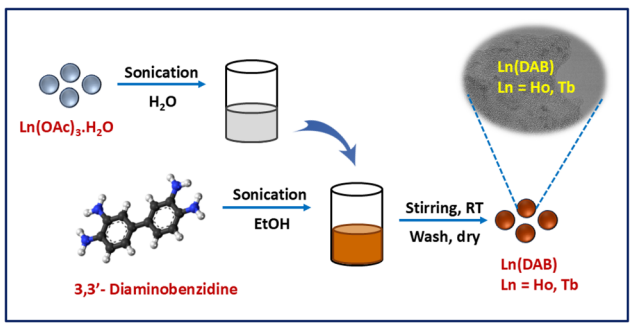

Fig. 1 Schematic for the synthesis of Ho(DAB) and Tb(DAB).

(1.8 g, 5 mmol) and $Tb(OAc)_3\square H_2O$ (1.7 g, 5 mmol), was combined with an ethanolic dispersion of DAB (1.1 g, 5 mmol) and stirred for 20 min at room temperature. The resulting precipitate was filtered and thoroughly washed with water and ethanol, followed by heating in ethanol at 60 °C in a hot air oven for 12 h. Finally, the precipitate was centrifuged with multiple washings using water and ethanol, yielding the COP as a dark-brown-coloured crystalline powder.

Characterization of COPs

A range of standard spectroscopic and electron microscopy techniques was employed to investigate the structure, morphology, and composition of the synthesized COPs. X-ray diffraction (XRD) analysis was conducted using a Rigaku Smart Lab X-ray diffractometer with CuKα radiation. Raman spectroscopy and FTIR spectroscopy were performed with a Horiba Jobin Yvon XploRA PLUS V1.2 MULTILINE using 532 nm excitation and a PerkinElmer Spectrum 1000 FT-IR spectrometer, respectively. UV-Vis spectra of the COPs were recorded using a Lambda 750 PerkinElmer UV-Vis spectrometer. Elemental and compositional analysis was carried out through X-ray photoelectron spectroscopy (XPS), conducted with a PHOBIOS 100/150 Delay Line Detector (DLD), with an Al Kα (1486.6 eV) dual anode as the source with a power of 385 W and anode voltage of 13.85 kV. The sample current measured with a pico-ammeter was found to be 175.6 nA on the sample surface. The XPS was taken with a pass energy of 50 eV. As an internal reference for the absolute binding energy, the C-1s peak (284.5 eV) was used. The structural, morphological, and compositional features were further examined with field emission scanning electron microscopy (FESEM) coupled with energy-dispersive spectroscopy (EDS) on a Carl Zeiss Supra 55, as well as high-resolution transmission electron microscopy (HRTEM) using Thermo Fisher Scientific Talos F200S G2.

Fluorometric detection of explosives

The synthesized Ln-COPs were utilized for the fluorometric detection of HEMs using a Shimadzu RF-6000 spectrophotometer. For the emission studies, a dispersion of 2 mg of Ln-COP in 10 mL of DMF was prepared. Fluorescence quenching studies were conducted using a titration approach, where the gradual decrease in the emission intensity was observed as a function of the quencher concentration. Explosive sensing was performed by adding incremental amounts of PNP, TNP, TNT, RDX, PETN, and CL-20 solutions, prepared in acetone, to the Ln-COP dispersion. The photoluminescence intensity was recorded after each addition to monitor changes. The Stern–Volmer equation (eqn (1)) was applied to assess the quenching efficiency, and the limit of detection (LOD) was calculated using eqn (2).

$$\frac{I_0}{I} = 1 + K_{sv}\,[Q] \quad (1)$$

$$\mathrm{LOD} = \frac{3\sigma}{m} \quad (2)$$

where I_0 and I are the initial and final fluorescence intensities before and after the addition of the analyte, K_{sv} is the Stern–Volmer constant, $[Q]$ is the concentration of the analyte, σ denotes the standard deviation of the blank, and m is the slope of the Stern–Volmer plot. Additionally, fluorescence lifetime measurements were performed for both the pristine Ln-COP solution and the quencher-added solutions using a time-resolved fluorescence spectrometer (Fluorolog HORIBA).

Results and discussion

Structural, morphological, and spectroscopic characterization of Ho(DAB) and Tb(DAB)

Fig. 2a presents the X-ray diffraction (XRD) patterns for the ligand (DAB) and the as-synthesized COPs, Ho(DAB) and Tb(DAB), respectively. In the XRD pattern of DAB (black trace), peaks are observed at 2θ values of 16.2°, 18.2°, 19.6°, 23.8°, 26.7°, 27.8°, 31.6°, and 33.9°, corresponding to the (011), (−111), (111), (020), (−112), (−121), (−221), and (−122) crystal planes, respectively. As observed in previous reports, Ln-COPs do not exhibit a complete change in their XRD pattern upon formation. Instead, they show a partial modification, where key reflections from the original ligand remain present but with noticeable shifts in the positions and intensities of certain peaks.[32–34] The XRD patterns of Ho(DAB) and Tb(DAB) (red and blue traces, respectively) reveal the crystallinity of the materials, with the major reflections corresponding to DAB. In the case of Tb(DAB), a complete shift in the crystal planes is observed, indicating structural changes or strain within the crystal lattice upon coordination. This shift suggests modifications in the arrangement of the molecular structure, which could be attributed to the formation of the COP.[35,36]

Fig. 2b presents the FTIR spectra of the ligand (black trace), alongside the Ln-COPs, Ho(DAB) (red trace) and Tb(DAB) (blue trace). Significant spectral changes are observed in the fingerprint region (1500–400 cm^{-1}) of the Ln-COPs compared to the observations for DAB, indicating the coordination between the Ln metal nodes and the nitrogen atoms of DAB.[37] The peaks around 1260 cm^{-1} and 1620 cm^{-1} for the Ln-COPs are assigned to C–N and C–C stretching, respectively.[38] In DAB, the sharp peaks at 3350 cm^{-1} and 3395 cm^{-1} correspond to the symmetric and asymmetric stretching of free amine groups. In contrast, these peaks broaden in the Ln-COPs, suggesting an N-4 interaction as a result of metal–nitrogen coordination in the complex.[28,39]

The Raman spectra of the Ln-COPs, presented in Fig. 2c (red and blue traces), differ significantly from that of the ligand (black trace). Notably, two prominent bands at ∼1350 cm^{-1} and ∼1550 cm^{-1} emerge, which are comparable to the D and G bands typically observed in graphitic (2D) materials, respectively. In graphitic structures, the G band is associated with C–C stretching in sp^2 carbon atoms, while the D band represents the breathing modes of sp^2 carbon atoms and is a double-resonance band arising from one-phonon lattice vibrations.[40–42] Additionally, a broad band at ∼2880 cm^{-1} indicates the presence of multiple stacked layers within the COP. These findings suggest that the synthesized COPs have a 2D

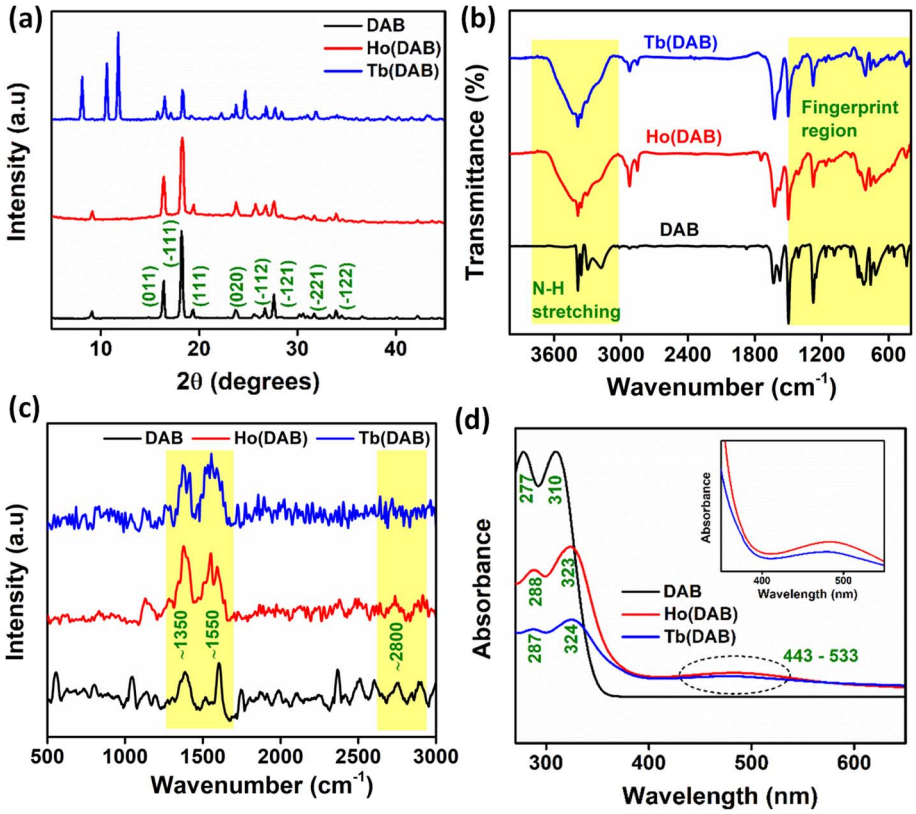

Fig. 2 (a) X-ray diffractograms; (b) FTIR spectra; (c) Raman spectra; and (d) UV-Vis spectra of DAB (black trace), Ho(DAB) (red trace), and Tb(DAB) (blue trace).

layered structure, further confirmed by the FESEM and HRTEM images discussed in subsequent sections.

The UV-Vis spectra of the ligand and the COPs are depicted in Fig. 2d. The ligand spectrum exhibits two absorption peaks at 277 nm and 310 nm, attributed to the $\pi \rightarrow \pi^*$ and $n \rightarrow \pi^*$ transitions, respectively, due to the presence of aromatic rings and heteroatoms (nitrogen) with a lone pair of electrons. Although the Ln-COP spectra are similar to those of DAB, a pronounced bathochromic shift indicates extended π-conjugation within the COPs. This is likely due to the polymerization of continuous, infinitely long 1D coordination strands stabilized by hydrogen bonds. An additional broad band centered around 443–533 nm is observed (Fig. 2d, inset). While the exact origin of this peak is currently unclear, it may be the result of charged species generated by the complex upon interaction with solvent molecules or from charge transfer between the lanthanide metal node and the ligand, as suggested by previous reports.[43–45]

The chemical composition and elemental states in the Ln-COPs were examined using X-ray photoelectron spectroscopy (XPS). The survey spectrum of Ho(DAB), presented in Fig. 3a, reveals distinct peaks at binding energies of 284.1 eV, 397.6 eV, 530.1 eV, and 974.5 eV, corresponding to the C 1s, N 1s, O 1s, and Ho 3d regions, respectively. High-resolution scans for these peaks, shown in Fig. 3b–e, provide detailed insights into the elemental composition, chemical states, and bonding environments within the COP.

The high-resolution C 1s spectrum (Fig. 3b) displays peaks at 284.2 eV, 284.5 eV, and 285.5 eV. The peaks at 284.2 eV and 285 eV are attributed to the C–C and C=C bonds,[46,47] primarily associated with the aromatic ring structure of the DAB ligand. Meanwhile, the peak at 285.5 eV corresponds to the C–N bonds, which are also present in the DAB molecule.[48,49] The N 1s spectrum (Fig. 3c) reveals distinct nitrogen environments in the material. A peak at 398 eV corresponds to C–NH bonds from the sp^3-hybridized nitrogen in the DAB moiety, while another peak at 399 eV indicates the presence of N–H bonds.[50,51] In the O 1s spectrum (Fig. 3d), peaks at 530.6 eV and 531.7 eV are associated with OH–O and OH–H_2O interactions, respectively, reflecting the presence of adsorbed and surface-bound water molecules.[52,53] The high-resolution Ho 4d spectrum (Fig. 3e) shows two distinct peaks resulting from spin–orbit splitting, corresponding to Ho $4d_{5/2}$ (161.7 eV) and Ho $4d_{3/2}$ (163.5 eV), accompanied by a satellite peak.[54] The peaks suggest the presence of Ho as Ho^{3+} in the COP.

The survey spectrum of Tb(DAB), shown in Fig. 4a, displays characteristic peaks at binding energies of 285.1 eV, 398.6 eV, 531.6 eV, and 1222.6 eV, corresponding to the C 1s, N 1s, O 1s, and Tb 3d regions, respectively. The C 1s high-resolution spectrum (Fig. 4b) exhibits peaks at 284 eV, 284.5 eV, and 286 eV. The peaks at 284 eV and 284.5 eV are attributed to the C–C and C=C bonds, respectively, originating from the aromatic ring structure of the DAB ligand.[46,47] The peak at 286 eV corresponds to the C–N bonds present in the DAB

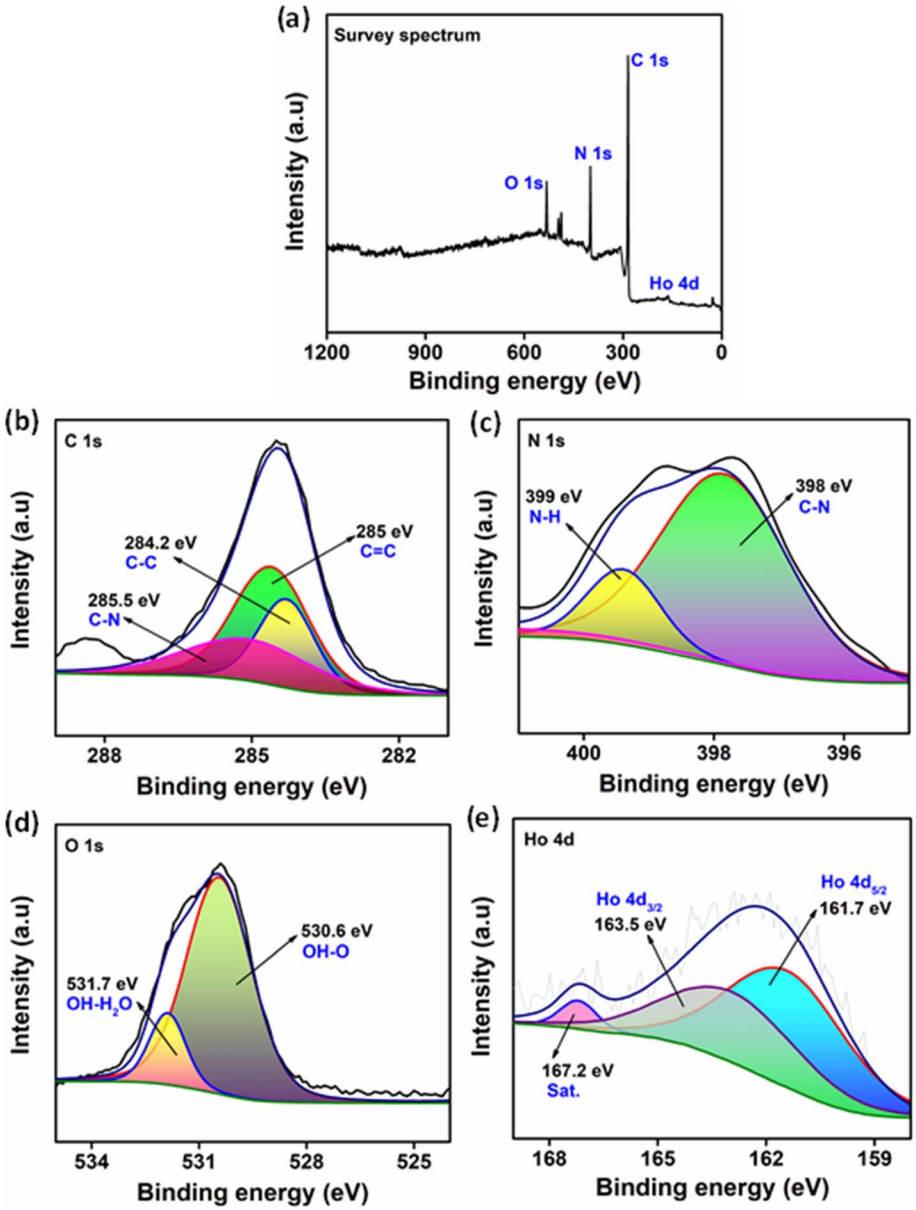

Fig. 3 (a) XPS survey spectrum of Ho(DAB). High-resolution core spectra, indicating (b) C 1s, (c) N 1s, (d) O 1s and (e) Ho 4d regions.

molecule.[48,49] In the N 1s spectrum (Fig. 4c), the peak at 398 eV is assigned to the C–NH bonds, representing sp^3-hybridized nitrogen in the DAB moiety. Additionally, a peak at 399 eV indicates the presence of N–H bonds in DAB.[50,51]

The O 1s spectrum (Fig. 4d) reveals peaks at 530.4 eV and 530.8 eV, corresponding to the OH–O and OH–H_2O interactions, respectively, indicating the presence of adsorbed and surface-bound water molecules.[52,53] The Tb 3d high-resolution spectrum (Fig. 4e) shows two distinct peaks due to spin–orbit splitting, located at 1235 eV and 1270 eV, representing the Tb $3d_{5/2}$ and Tb $3d_{3/2}$ levels, respectively.[55,56] These peaks confirm the Tb(III) oxidation state within the COP.

Field-emission scanning electron microscopy (FESEM) was used to obtain images and provide detailed information about the morphology of the samples. Fig. 5a and b presents FESEM images of the synthesized COPs, Ho(DAB), and Tb(DAB), respectively. The images reveal that the COPs consist of thin, planar 2D layers stacked atop each other. These smooth, sheet-like structures are associated with the formation of thick bundles. As previously mentioned, these planar 2D layers result from the self-assembly of indefinitely long COP strands stabilized by hydrogen bonds. To further analyze the elemental composition of the COPs, energy-dispersive X-ray spectroscopy (EDS) was employed, determining the weight percentages of C, N, and Ho in Ho(DAB) and those of C, N, and Tb in Tb(DAB). The EDS spectra of Ho(DAB) and Tb(DAB) are depicted in Fig. S1 and S2, respectively.

High-resolution transmission electron microscopy (HRTEM) was utilized to examine the COPs' crystallographic structure. The HRTEM images in Fig. 5c and d support the FESEM

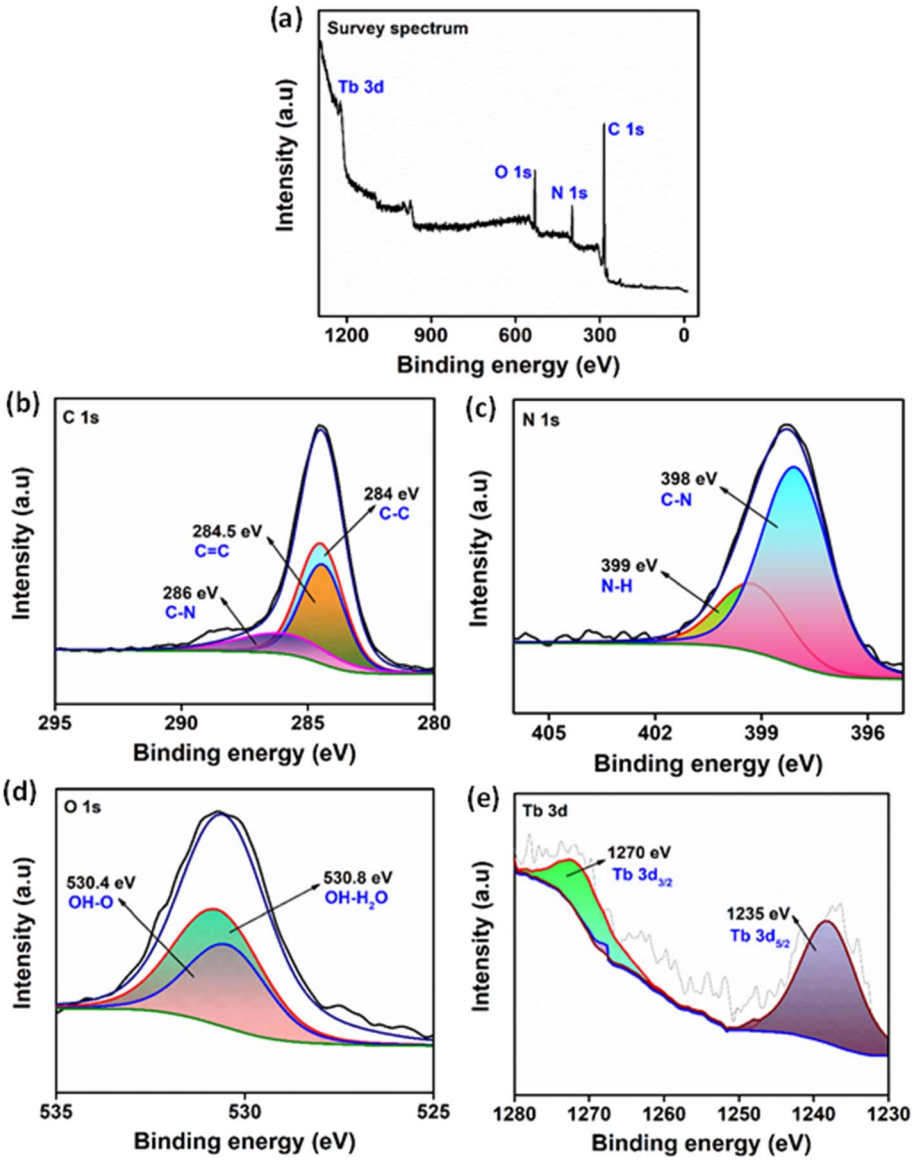

Fig. 4 (a) XPS survey spectrum of Tb(DAB). High-resolution core spectra, indicating (b) C 1s, (c) N 1s, (d) O 1s and (e) Tb 3d regions.

findings, showing that the COPs comprise extensive bundles of planar 2D sheets. Additionally, high-angle annular dark-field (HAADF) scanning transmission electron microscopy (STEM) was performed to map the distribution of elements within the as-synthesized Ln-COPs. Fig. 5e and f shows the HAADF-STEM image, along with elemental mapping of C, N, Ho in Ho(DAB) (Fig. S3) and C, N, Tb in Tb(DAB) (Fig. S4), which illustrate the even distribution of these elements throughout the proposed layered 2D structure. The discrepancy in oxygen detection among FESEM-EDS, HAADF-STEM, and XPS can be attributed to the fundamental differences in these techniques. XPS is highly surface-sensitive, probing only the top few nanometers of a sample, and it can detect oxygen from adsorbed species or contaminants. In contrast, FESEM-EDS and HAADF-STEM analyze a larger volume, often extending to the bulk of the material. As a result, oxygen confined to the surface may not be detected if its concentration in the bulk is low.

Based on previous literature reports and our comprehensive characterization results, a plausible structural representation of the Ln-COPs is proposed and shown in Scheme 1. It is believed that the Ln^{3+} ions coordinate with the N atoms of DAB ligands, leading to the formation of one-dimensional (1D) coordination polymeric chains. This coordination is consistent with the Hard and Soft Acids and Bases (HSAB) principle, where the Ln^{3+} ions (hard acids) preferentially bind to the amine N atoms of DAB (hard bases). These 1D chains are further stabilized through intermolecular hydrogen bonding interactions, particularly involving the $-NH_2$ groups of DAB, which drive the formation of two-dimensional (2D) layered architectures. In instances where the coordination environment of the Ln^{3+} ions remains incomplete, H_2O molecules serve as auxiliary ligands, occupying the vacant coordination sites and enhancing the structural integrity.

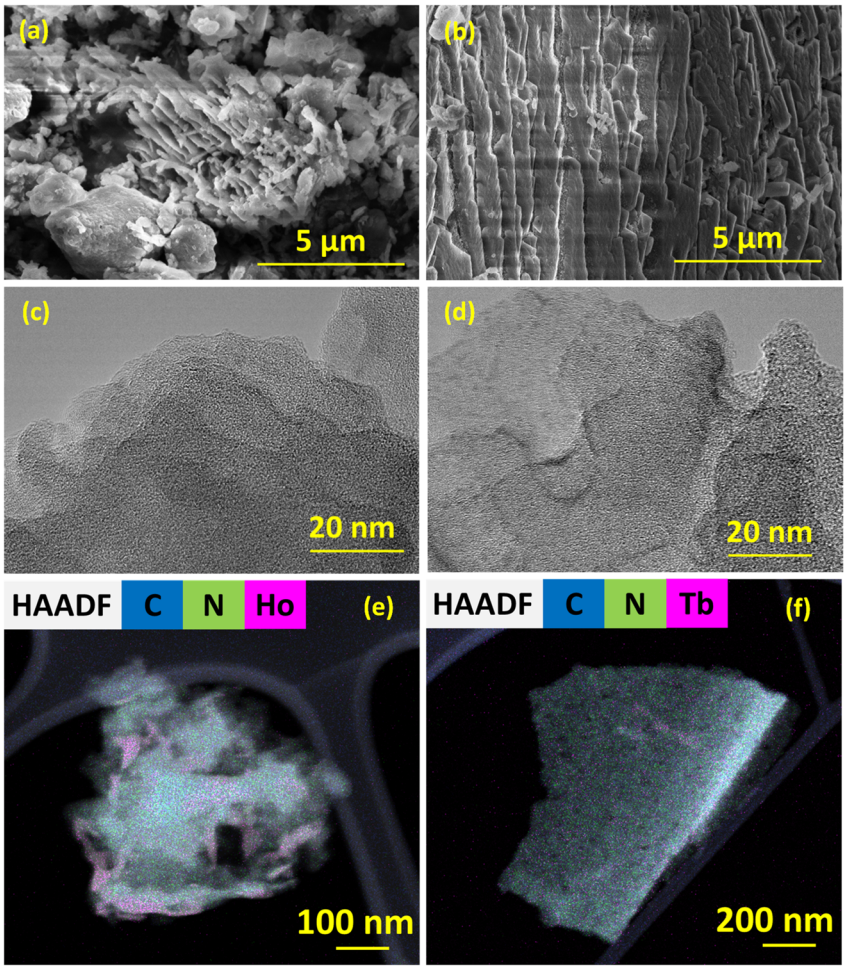

Fig. 5 (a and b) FESEM images; (c and d) HRTEM images; and (e and f) HAADF-STEM images of Ho(DAB) and Tb(DAB), respectively.

Photophysical properties of Ho(DAB) and Tb(DAB)

The Ln-COPs, Ho(DAB) and Tb(DAB) intrinsically exhibited fluorescence emission in their suspended state (in DMF) upon irradiation with UV light of suitable excitation wavelength. Fig. 6a and b depicts the combined absorption-emission spectra of Ho(DAB) and Tb(DAB), respectively. The emission peak appears to have red-shifted relative to the absorption peak, with a Stokes shift of ~85 nm, obtained using eqn (3).

$$\text{Stokes shift} = \lambda_{\text{absorption}} - \lambda_{\text{emission}} \quad (3)$$

where $\lambda_{\text{absorption}}$ and $\lambda_{\text{emission}}$ are the wavelengths of maximum absorption and maximum emission in the COP. The Stokes shift corresponds to energy lost due to non-radiative processes before the Ln-COP emits a photon. A shift of 85 nm indicates a significant energy loss during the vibrational relaxation process. This may be due to the intramolecular charge transfer occurring in the Ln-COPs.[57]

The fluorescence mechanism in COPs involving Ln(III) metal centers, such as Ho(III) and Tb(III), relies on the antenna effect, also known as the sensitization of lanthanide complexes. In this process, the organic π-conjugated ligand (DAB, here) absorbs light energy and transitions to its singlet excited state. This energy is then transferred to the ligand's long-lived triplet state through intersystem crossing. Subsequently, the triplet state transfers the energy to the excited states of the Ln(III) ions, which emit their characteristic fluorescence. The antenna effect is critical because lanthanides have weak direct absorption in the UV-visible region due to parity-forbidden f–f transitions.[58–60] The ligand serves as an "antenna", efficiently harvesting light and transferring energy to the lanthanide center. Moreover, the Ln(III) ions actively quench the triplet state of the ligand, minimizing photobleaching and enhancing the photostability of the system.[61]

The surrounding environment of the COPs, including interactions with other organic or inorganic systems, significantly impacts the energy transfer and fluorescence emission by affecting the triplet state of the ligand or the efficiency of the energy migration process. This property has practical applications, such as detecting electron-deficient HEMs, as we shall discuss further. The quantum yield of the Ln-COPs was determined to assess their fluorescence properties (Table S1). Specifically, Ho(DAB) exhibited a quantum yield of 7.49%, while Tb(DAB) demonstrated a higher quantum yield of 12.79%. The process for calculating these values, along with the

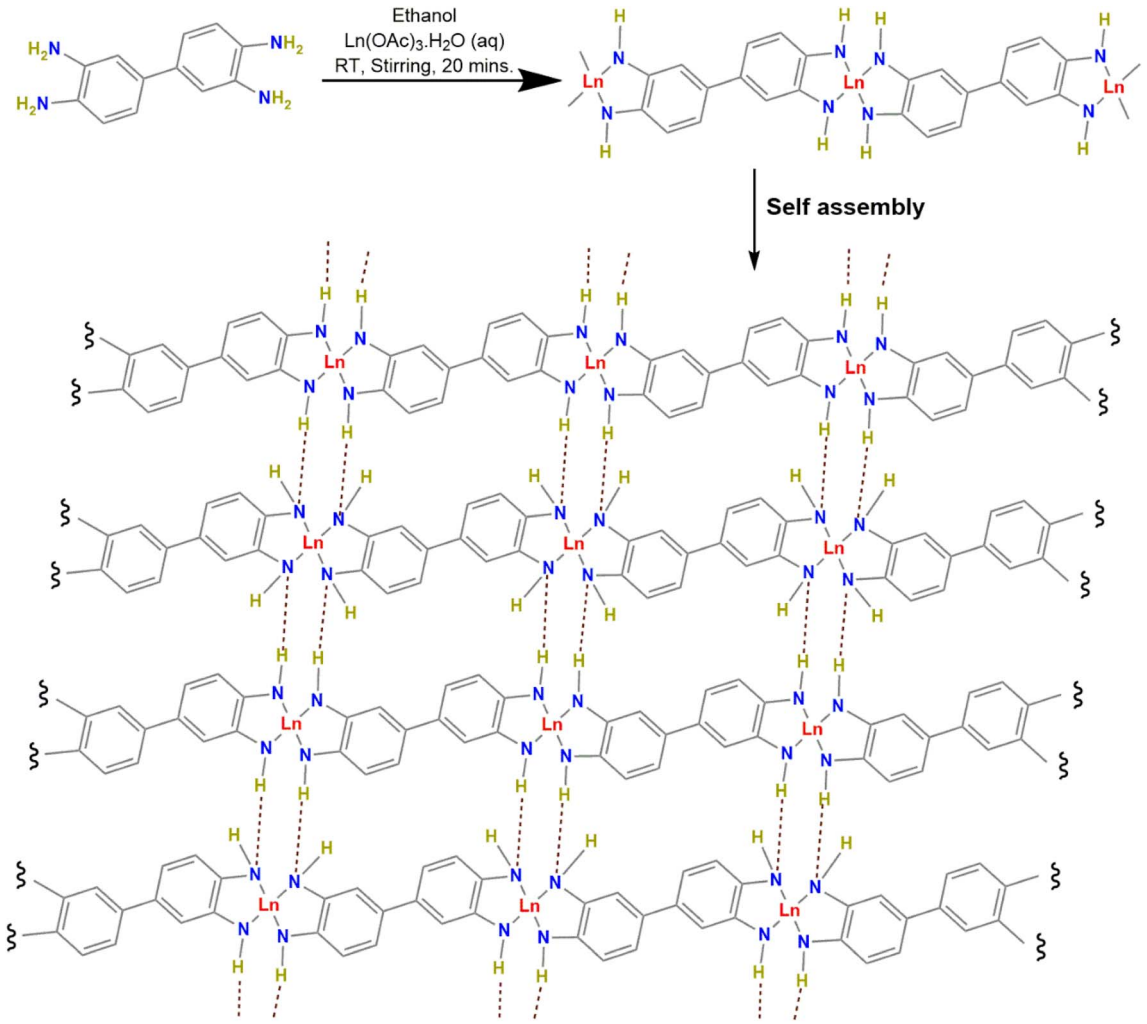

Scheme 1 Scheme for the synthesis of Ln-COPs (Ln = Ho and Tb).

corresponding plots (Fig. S5), can be found in SI. These calculations involve analyzing the fluorescence intensity and comparing the sample's emission to a standard (quinine sulfate), providing insights into the efficiency of the fluorescence emission of these compounds (eqn (S1)).

Fig. 6c and d show the photoluminescence emission spectra of Ho(DAB) and Tb(DAB) at different excitation wavelengths. From the spectra, it is evident that the Ln-COPs show maximum emission at excitation wavelengths (λ_{ex}) 368 nm and 367 nm for Ho(DAB) and Tb(DAB), respectively.

The quenching experiments were conducted on solutions of Ln-COPs dispersed in DMF. 2 mg of the COP sample was dispersed in DMF (10 mL) and subjected to sonication for 10 minutes to achieve a uniform dispersion, which was then utilized for subsequent studies (1.5 mL for PNP, TNP, TNT and 2 mL for RDX, PETN, CL-20). Quenching solutions were prepared by dissolving predetermined amounts of various HEMs in acetone to attain the desired concentrations. These solutions were used for titration experiments with the fluorophore. A range of nitroaromatics and HEMs typically associated with explosives was selected for the study. These included PNP, TNP, TNT, RDX, PETN, and CL-20. Fluorometric titrations were conducted by incrementally adding precise amounts of HEM solutions to the fluorophore-containing solution until no further decrease in fluorescence intensity was observed, and the resulting fluorescence responses were recorded. The fluorescence quenching was analyzed as a function of the quencher concentration. To evaluate the steady-state fluorescence quenching, the data were fitted using the Stern–Volmer equation.

The fluorescence quenching study of Ho(DAB) was conducted using six different quenchers, *viz.*, nitroaromatics (*e.g.*, PNP, TNP, and TNT) and non-nitroaromatics (*e.g.*, RDX, PETN, and CL-20). The quenching profiles obtained and their corresponding Stern–Volmer plots are depicted in Fig. 7 and 8. The Stern–Volmer plots for nitroaromatics (Fig. 7) display a small hump at lower quencher concentrations, followed by a linear region. This can be attributed to strong π–π interactions or charge–transfer interactions between the electron-deficient nitroaromatics and the electron-rich fluorophores. This results in an initial static quenching contribution, which transitions to a dynamic quenching process as the concentration

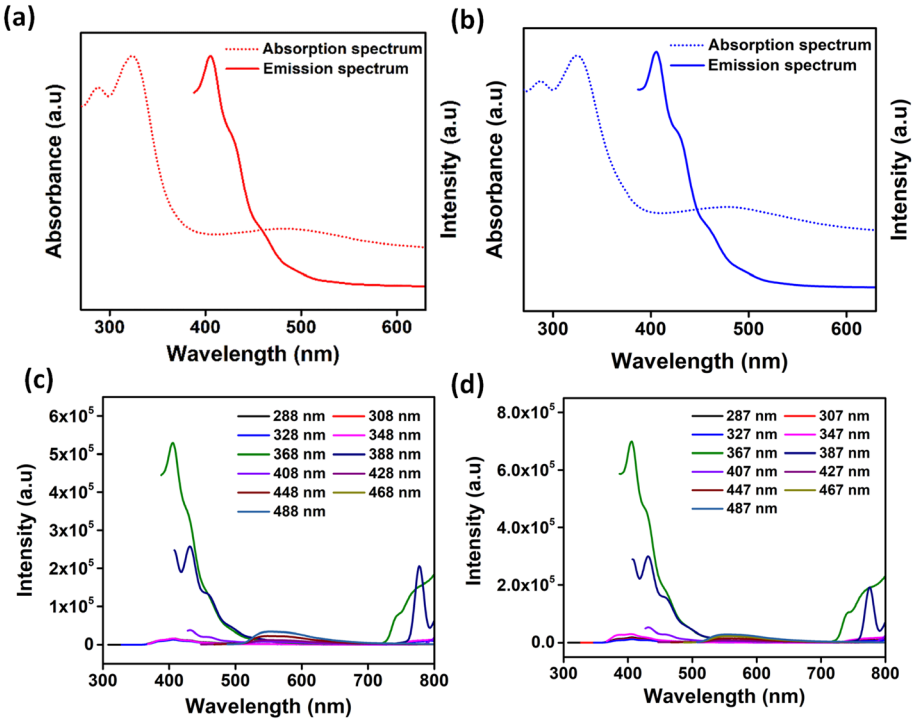

Fig. 6 Overlaid normalized absorption–emission spectra for (a) Ho(DAB) and (b) Tb(DAB). Photoluminescence emission spectra of (c) Ho(DAB) and (d) Tb(DAB) at different excitation wavelengths.

increases.[62,63] Among the nitroaromatics studied, PNP exhibited the highest quenching efficiency, as reflected by its elevated K_{sv}, indicating strong interactions with the fluorophore. On the other hand, TNP showed the highest sensitivity, characterized by its remarkably low LOD, measured at 16.4 μM. This suggests that TNP can be detected and quantified at much lower concentrations than other nitroaromatics, highlighting its enhanced compatibility with the sensing material and its significant impact on fluorescence quenching even at minimal concentrations.

For non-nitroaromatics (Fig. 8), the Stern–Volmer plots show a deviation from linearity without the presence of notable humps, suggesting a more complex quenching mechanism. Unlike nitroaromatics, non-nitroaromatics lack strong electron-withdrawing groups, such as nitro groups, which are responsible for charge–transfer interactions.[64] As a result, the quenching is less uniform, possibly involving weaker and less specific interactions, leading to the observed nonlinear trend. The absence of humps suggests minimal contributions from significant static quenching, indicating that the observed quenching likely arises from a combination of static and dynamic processes operating at varying rates. Among the non-nitroaromatic HEMs, PETN demonstrated the highest sensitivity and efficiency, with a K_{sv} of 5.01 × 10^3 M^{-1} and LOD of 28.9 μM. CL-20 also exhibited comparable results, while RDX showed higher LOD values. Fig. S6 shows images of the quenched solutions under both visible and UV light conditions.

To facilitate comparative analysis, another Ln-COP, synthesized using terbium (Tb) as the metal center, designated as Tb(DAB), was evaluated for its chemosensing capabilities towards HEMs. The experimental protocols and explosives used for the study were consistent with those previously described. The fluorescence quenching plots for Tb(DAB) are presented in Fig. S7 and S8. The sensing behavior of Tb(DAB) closely followed the trend observed for Ho(DAB). The nitroaromatic explosives, including PNP, TNP, and TNT, exhibited a higher degree of fluorescence quenching compared to the non-nitroaromatic explosives, such as RDX, PETN, and CL-20. TNP demonstrated the highest quenching efficiency and sensitivity, as reflected by its K_{sv} value of 2.09 × 10^4 M^{-1} and its LOD of 7.7 μM. Among the non-nitroaromatic HEMs, PETN exhibited the best sensing performance, with results comparable to those of RDX and CL-20. Fig. S9 shows images of the quenched solutions under both visible and UV light conditions. Table 1 summarizes the sensing parameters for all HEMs, including K_{sv} and LODs, obtained using both Ho(DAB) and Tb(DAB).

A graphical representation of the quenching efficiency obtained for all HEMs is shown in Fig. S10. Table S2 summarizes reports of studies focusing on fluorometric detection of HEMs using Ho- and Tb-based COPs. Although the studies observe low detection limits for Tb-based COPs, most are specifically limited to TNP detection and do not target non-nitroaromatic compounds. However, Ho-based COPs remain unexplored to date.

Mechanistic insights into the interaction between HEMs and Ln-COPs

The interactions between HEMs and Ln-COPs involve complex mechanisms primarily driven by both static and dynamic

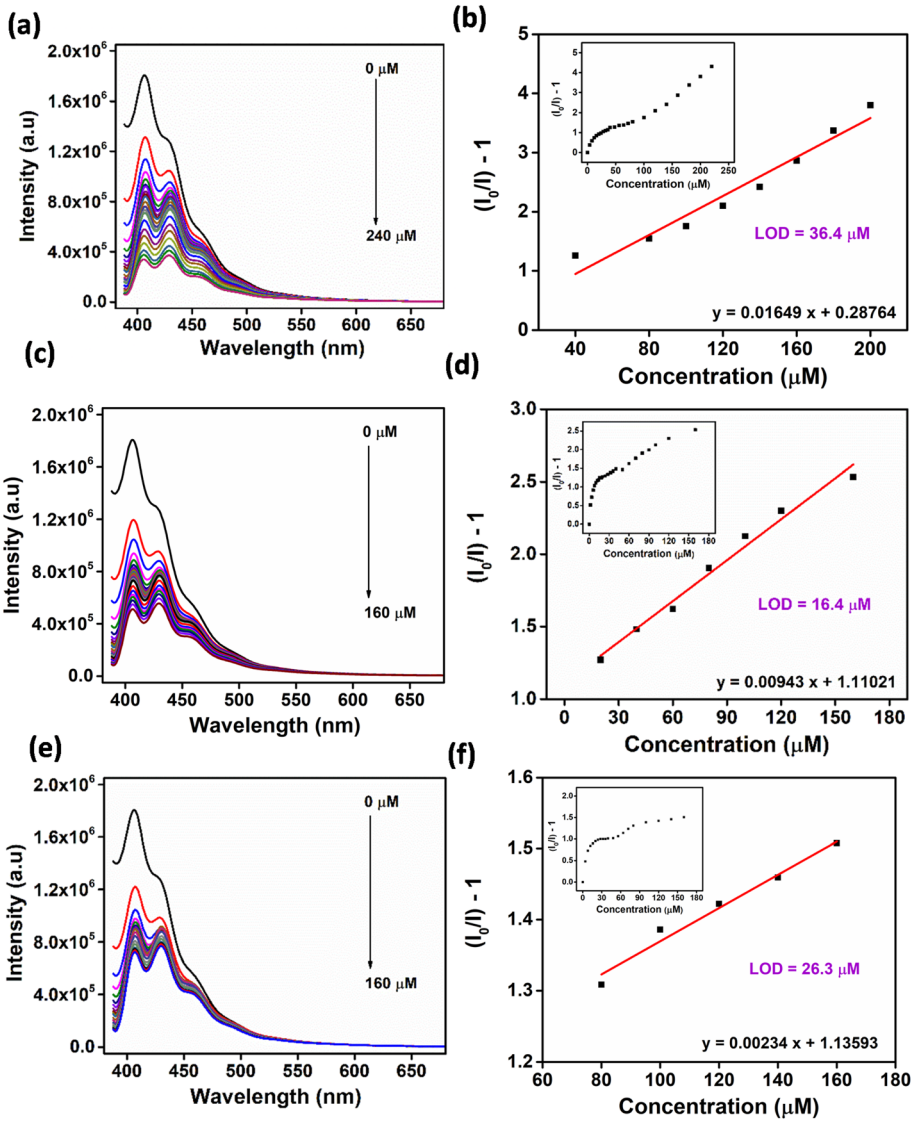

Fig. 7 Fluorescence spectra of Ho(DAB) suspended in DMF, recorded following the stepwise addition of micromolar concentrations of (a and b) PNP, (c and d) TNP, and (e and f) TNT dissolved in acetone, along with their corresponding Stern–Volmer plots.

quenching processes. As previously discussed, the presence of a hump at low concentrations in the Stern–Volmer plot suggests the predominance of static quenching, where the explosive molecules form a ground-state complex with the Ln-COPs. The absence of spectral overlap between the emission of the Ln-COPs and the absorption of the explosives (as shown in Fig. S11) eliminates the possibility of energy-transfer mechanisms, such as Förster resonance energy transfer (FRET).[65]

Instead, the quenching mechanism is attributed to the interaction of explosive molecules with the ground state of the Ln-COPs, preventing fluorescence without involving excited-state processes. At lower quencher concentrations, static quenching dominates, which results in the nonlinear behavior observed in the Stern–Volmer plot. The corresponding decrease in UV absorbance upon the addition of explosives, as illustrated in Fig. S12 and S13, further corroborates the static quenching hypothesis. This reduction in absorbance can be interpreted as a modification of the electronic structure of the Ln-COPs due to the ground-state interaction with the explosives, which diminishes the capacity of the Ln-COPs to absorb light at their characteristic wavelengths. At higher quencher concentrations, dynamic quenching plays a more significant role, where collisions between the explosive molecules and the excited-state Ln-COPs lead to fluorescence quenching *via* non-radiative processes, thereby producing a linear portion in the Stern–Volmer plot.[66]

To further validate the dominance of static quenching, fluorescence lifetime decay analysis was performed for both Ho(DAB) and Tb(DAB) in the presence and absence of the quencher. As seen in Fig. 9a and b, the fluorescence lifetime remains nearly constant despite the addition of the explosive, reinforcing the idea of static quenching. Since static quenching involves the formation of a non-fluorescent ground-state complex, the fluorescence lifetime remains unaffected by the

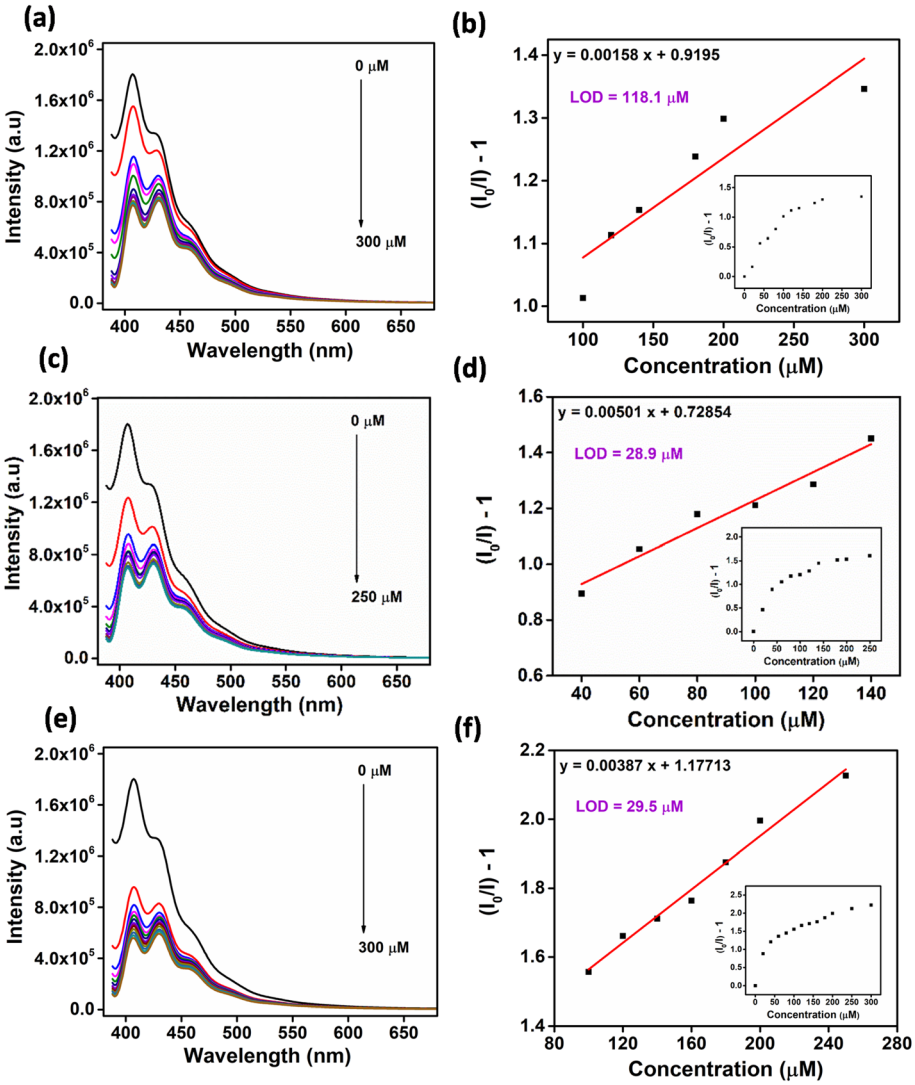

Fig. 8 Fluorescence spectra of Ho(DAB) suspended in DMF, recorded following the stepwise addition of micromolar concentrations of (a and b) RDX, (c and d) PETN, and (e and f) CL-20 dissolved in acetone, along with their corresponding Stern–Volmer plots.

Table 1 Sensing parameters of HEMs using Ln-COPs derived from Stern–Volmer plots

	Ho(DAB)		Tb(DAB)	
HEM	K_{sv} (M^{-1})	LOD (μM)	K_{sv} (M^{-1})	LOD (μM)
PNP	1.65×10^4	36.4	9.12×10^3	10.3
TNP	9.43×10^3	16.4	2.09×10^4	7.7
TNT	2.34×10^3	26.3	9.04×10^2	115.8
RDX	1.58×10^3	118.1	3.49×10^3	24.8
PETN	5.01×10^3	28.9	5.53×10^3	12.4
CL-20	3.87×10^3	29.5	4.54×10^3	46.5

quencher concentration, as no dynamic processes (such as collision-induced quenching) occur in the excited state.[67] Detailed calculations of the average lifetime are provided in SI. From the average lifetimes of Ln-COPs before and after the addition of TNP (Table S3), it is evident that Tb(DAB) specifically shows an increase of 0.1 ns. This may be attributed to the altered equilibrium between the ground-state complex and the free fluorophore.

Thus, the observed quenching behavior of the Ln-COPs, Ho(DAB) and Tb(DAB), with nitroaromatic compounds can be attributed to the formation of ground-state charge-transfer complexes, where electron transfer occurs from the COP framework to the electron-deficient nitroaromatic molecules. The nitro groups (–NO_2) in compounds such as PNP, TNP and TNT act as strong electron-withdrawing groups, enhancing the tendency for electron transfer from the ligand to the analyte. Additionally, hydrogen-bonding interactions between the uncoordinated nitrogen (N) atoms in the DAB ligand and oxygen atoms (O) from uncoordinated water molecules play a crucial role in stabilizing these complexes. The interaction between the π-systems of the COP ligands and the aromatic rings of the nitroaromatics further strengthens the overall quenching mechanism through π–π stacking. In contrast, non-

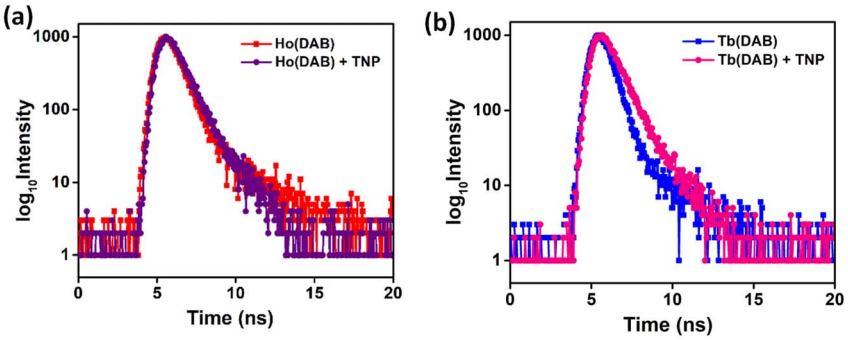

Fig. 9 Fluorescence lifetime decay of (a) Ho(DAB) and Ho(DAB) + TNP (b) Tb(DAB) and Tb(DAB) + TNP.

nitroaromatics exhibit weaker quenching due to their relatively less electron-deficient nature, resulting in fewer and less efficient interactions with the COPs. These results highlight the synergistic role of hydrogen bonding, π–π stacking, and electron transfer in dictating the quenching efficiency, with nitroaromatics showing superior quenching due to their multifaceted interactions with the Ln-COPs.[68,69] Specifically, for TNT, the LOD is significantly lower in Ho(DAB) than in Tb(DAB), which can be attributed to the lanthanide contraction in Ho. The smaller ionic radius of Ho^{3+} leads to a tighter packing of the 1D chains and more favorable stacking interactions, enhancing the electron-transfer process[70,71] and ultimately contributing to a more efficient quenching effect at lower analyte concentrations.

Conclusion

This study reports the synthesis and detailed characterization of two novel Ln-COPs constructed from an N-4 ligand and Ho(III)/Tb(III) ions. The developed synthetic approach is straightforward, highly efficient, and easily scalable. A comprehensive analysis of the COPs' compositions and morphologies was performed using advanced spectroscopic and microscopic techniques. XRD confirmed the crystalline structure of the materials, while FESEM and HRTEM revealed their distinctive two-dimensional layered morphology. The Ln-COPs demonstrated excellent photophysical properties, particularly for the detection of HEMs. The remarkable fluorescence quenching performance, particularly the low LODs of 16.4 μM and 7.7 μM for TNP achieved by Ho(DAB) and Tb(DAB), respectively, highlights the potential of these materials for practical applications in detecting both nitroaromatic and non-nitroaromatic explosives.

Author contributions

Samika Anand: Data curation, conceptualization, methodology, investigation, writing-original draft. Abhishek Kumar: Methodology, data curation, formal analysis. Kalathiparambil Rajendra Pai Sunajadevi: Conceptualization, supervision, project administration, validation, writing-review and editing. Channabasaveshwar V. Yelamaggad: Conceptualization, resources, supervision, writing-review and editing, validation. Kaustava Bhattacharyya: Data curation, formal analysis.

Conflicts of interest

The authors declare no competing financial interest.

Data availability

The data supporting this article have been included as part of the supplementary information (SI). Supplementary information is available. See DOI: **https://doi.org/10.1039/d5ra02731d**.

Acknowledgements

The authors acknowledge the support of Christ University and Centre for Nano and Soft Matter Sciences (CeNS). Samika Anand is grateful to the Department of Science and Technology, Government of India, for providing the INSPIRE fellowship.

References

1 M. B. Talawar, R. Sivabalan, M. Anniyappan, G. M. Gore, S. N. Asthana and B. R. Gandhe, Emerging trends in advanced high energy materials, *Combust. Explos. Shock Waves*, 2007, **43**, 62–72.
2 J. I. Steinfeld and J. Wormhoudt, EXPLOSIVES DETECTION: A Challenge for Physical Chemistry, *Annu. Rev. Phys. Chem.*, 1998, **49**, 203–232.
3 Y. Ma, S. Wang and L. Wang, Nanomaterials for luminescence detection of nitroaromatic explosives, *TrAC Trends Anal. Chem.*, 2015, **65**, 13–21.
4 S. A. Ture, S. D. Pattathil, B. Z. Zing and V. Abbaraju, Fluorescence Sensing of Some Important Nitroaromatic Compounds by Using Polyaniline Ag Composite, *Micro*, 2023, **3**, 224–238.
5 S. Shanmugaraju and P. S. Mukherjee, π-Electron rich small molecule sensors for the recognition of nitroaromatics, *Chem. Commun.*, 2015, **51**, 16014–16032.
6 N. J. Duijm, Hazard analysis of technologies for disposing explosive waste, *J. Hazard. Mater.*, 2002, **90**, 123–135.
7 B. Sun, M. Li, F. Zhang, Y. Zhong, N. Kang, W. Lu and J. Liu, The performance of a fast testing system for illicit materials

detection based on energy-dispersive X-ray diffraction technique, *Microchem. J.*, 2010, **95**, 293–297.
8 J. F. Garcia-Reyes, J. D. Harper, G. A. Salazar, N. A. Charipar, Z. Ouyang and R. G. Cooks, Detection of Explosives and Related Compounds by Low-Temperature Plasma Ambient Ionization Mass Spectrometry, *Anal. Chem.*, 2011, **83**, 1084–1092.
9 A. Hakonen, P. O. Andersson, M. Stenbæk Schmidt, T. Rindzevicius and M. Käll, Explosive and chemical threat detection by surface-enhanced Raman scattering: A review, *Anal. Chim. Acta*, 2015, **893**, 1–13.
10 R. Ewing, A critical review of ion mobility spectrometry for the detection of explosives and explosive related compounds, *Talanta*, 2001, **54**, 515–529.
11 J. A. Threadgold, P. E. Fowler and G. A. Eiceman, Ultrafast Gas Chromatography-Tandem Differential Mobility Spectrometry: Toward A New Generation of On-Site, Real-Time Trace-Explosives Detection, *Anal. Chem.*, 2024, **96**(34), 13830–13837.
12 L. Karadurmus, S. Bilge, A. Sınağ and S. A. Ozkan, Molecularly imprinted polymer (MIP)-Based sensing for detection of explosives: Current perspectives and future applications, *TrAC Trends Anal. Chem.*, 2022, **155**, 116694.
13 K. C. To, S. Ben-Jaber and I. P. Parkin, Recent Developments in the Field of Explosive Trace Detection, *ACS Nano*, 2020, **14**, 10804–10833.
14 V. Desai, M. Panchal, S. Dey, F. Panjwani and V. K. Jain, Recent Advancements for the Recognization of Nitroaromatic Explosives Using Calixarene Based Fluorescent Probes, *J. Fluoresc.*, 2022, **32**, 67–79.
15 S. Paria, P. Maity, R. Siddiqui, R. Patra, S. B. Maity and A. Jana, Nanostructured Luminescent Micelles: Efficient "Functional Materials" for Sensing Nitroaromatic and Nitramine Explosives, *Photochem*, 2022, **2**, 32–57.
16 S. Mukhopadhyay, P. Mondal and P. Chattopadhyay, Covalent organic framework as fluorescent turn-on/off sensor and an account of operating sensing mechanism, *Inorganica Chim. Acta*, 2023, **546**, 121318.
17 S. Tajik, H. Beitollahi, F. G. Nejad, Z. Dourandish, M. A. Khalilzadeh, H. W. Jang, R. A. Venditti, R. S. Varma and M. Shokouhimehr, Recent Developments in Polymer Nanocomposite-Based Electrochemical Sensors for Detecting Environmental Pollutants, *Ind. Eng. Chem. Res.*, 2021, **60**, 1112–1136.
18 T. Zhao, F. Zhang, J. Zhou and X. Zhao, Luminescent Metal-Organic Frameworks for Nitroaromatic Compounds Detection, *Comments Inorg. Chem.*, 2021, **41**, 100–132.
19 X. Sun, Y. Wang and Y. Lei, Fluorescence based explosive detection: from mechanisms to sensory materials, *Chem. Soc. Rev.*, 2015, **44**, 8019–8061.
20 S. Shanmugaraju and P. S. Mukherjee, Self-Assembled Discrete Molecules for Sensing Nitroaromatics, *Chem.–Eur. J.*, 2015, **21**, 6656–6666.
21 S. Abednatanzi, P. Gohari Derakhshandeh, H. Depauw, F.-X. Coudert, H. Vrielinck, P. Van Der Voort and K. Leus, Mixed-metal metal–organic frameworks, *Chem. Soc. Rev.*, 2019, **48**, 2535–2565.
22 X.-H. Chang, Y. Zhao, M.-L. Han, L.-F. Ma and L.-Y. Wang, Five Cd(ii) coordination polymers based on 2,3′,5,5′-biphenyltetracarboxylic acid and N-donor coligands: syntheses, structures and fluorescent properties, *CrystEngComm*, 2014, **16**, 6417–6424.
23 J.-Q. Liu, Z.-D. Luo, Y. Pan, A. Kumar Singh, M. Trivedi and A. Kumar, Recent developments in luminescent coordination polymers: Designing strategies, sensing application and theoretical evidences, *Coord. Chem. Rev.*, 2020, **406**, 213145.
24 A. K. Ghosh, A. Hazra, A. Mondal and P. Banerjee, Weak interactions: The architect behind the structural diversity of coordination polymer, *Inorganica Chim. Acta*, 2019, **488**, 86–119.
25 T. Gorai, W. Schmitt and T. Gunnlaugsson, Highlights of the development and application of luminescent lanthanide based coordination polymers, MOFs and functional nanomaterials, *Dalton Trans.*, 2021, **50**, 770–784.
26 Y. Hasegawa and Y. Kitagawa, Luminescent lanthanide coordination polymers with transformative energy transfer processes for physical and chemical sensing applications, *J. Photochem. Photobiol., C*, 2022, **51**, 100485.
27 L. Han, S. G. Liu, Y. Z. Yang, Y. Z. Fan, J. Zhou, X. Y. Zhang, N. B. Li and H. Q. Luo, A lanthanide coordination polymer as a ratiometric fluorescent probe for rapid and visual sensing of phosphate based on the target-triggered competitive effect, *J. Mater. Chem. C*, 2020, **8**, 13063–13071.
28 S. A. Bhat and C. V. Yelamaggad, The Fluorometric Detection of Explosives: An Application of Photoluminiscent Coordination Polymers, *ACS Appl. Polym. Mater.*, 2022, **4**, 7126–7134.
29 S. Rahaman, M. B. Kanakala, M. Waldiya, A. Sadhanala, C. V. Yelamaggad and K. Pandey, Scalable novel lanthanide-ligand complex for robust flexible micro-supercapacitors, *J. Power Sources*, 2023, **564**, 232801.
30 S. A. Bhat, N. B. Palakurthy, N. Kambhala, A. Subramanian, D. S. Shankar Rao, S. Krishna Prasad and C. V. Yelamaggad, Gram-Scale Synthesis and Multifunctional Properties of a Two-Dimensional Layered Copper(II) Coordination Polymer, *ACS Appl. Polym. Mater.*, 2020, **2**, 1543–1552.
31 S. Anand, S. Devi Kalathiparambil Rajendra Pai, A. Kumar and C. V. Yelamaggad, Affordable Two-Dimensional Layered Cd(II) Coordination Polymer: High-Performance Pseudocapacitor Electrode Behavior, *ACS Omega*, 2024, **9**, 41807–41818.
32 X.-X. Wang, N. Ren, Y.-Y. Ma, L.-N. Geng and J.-J. Zhang, Synthesis, crystal structure, thermal behavior, and fluorescence property of lanthanide complexes based on 2,6-dimethylbenzoic acid and 1,10-phenanthroline, *Chem. Pap.*, 2022, **76**, 5267–5280.
33 M. Govindaraj, S.-Y. Zhong, C.-H. Lin and J.-D. Chen, Metal and Ligand Effect on the Structural Diversity of Divalent Coordination Polymers with Mixed Ligands: Evaluation for Photodegradation, *Molecules*, 2023, **28**, 2226.
34 E. R. Engel and J. L. Scott, Advances in the green chemistry of coordination polymer materials, *Green Chem.*, 2020, **22**, 3693–3715.

35 J.-P. Zhang, P.-Q. Liao, H.-L. Zhou, R.-B. Lin and X.-M. Chen, Single-crystal X-ray diffraction studies on structural transformations of porous coordination polymers, *Chem. Soc. Rev.*, 2014, **43**, 5789–5814.

36 C. Giannini, M. Ladisa, D. Altamura, D. Siliqi, T. Sibillano and L. De Caro, X-ray Diffraction: A Powerful Technique for the Multiple-Length-Scale Structural Analysis of Nanomaterials, *Crystals*, 2016, **6**, 87.

37 A. Kovács and W. Klotzbücher, Octa-coordination in complexes of lanthanides with N2 confirmed by matrix-isolation IR spectroscopy and DFT calculations, *J. Mol. Struct.*, 2023, **1272**, 134222.

38 M. Karabacak, S. Bilgili and A. Atac, Molecular structure, spectroscopic characterization, HOMO and LUMO analysis of 3,3′-diaminobenzidine with DFT quantum chemical calculations, *Spectrochim. Acta, Part A*, 2015, **150**, 83–93.

39 J. K. Cooper, A. M. Franco, S. Gul, C. Corrado and J. Z. Zhang, Characterization of Primary Amine Capped CdSe, ZnSe, and ZnS Quantum Dots by FT-IR: Determination of Surface Bonding Interaction and Identification of Selective Desorption, *Langmuir*, 2011, **27**, 8486–8493.

40 C. Wu, L. Dong, J. Huang and P. T. Williams, Optimising the sustainability of crude bio-oil *via* reforming to hydrogen and valuable by-product carbon nanotubes, *RSC Adv.*, 2013, **3**, 19239.

41 H. Liu, T. Kuila, N. H. Kim, B.-C. Ku and J. H. Lee, In situ synthesis of the reduced graphene oxide–polyethyleneimine composite and its gas barrier properties, *J. Mater. Chem. A*, 2013, **1**, 3739.

42 I. Childres, L. A. Jaureguib, W. Parkb, H. Caoa and Y. P. Chena, in *New Developments in Photon and Materials Research*, 2013, pp. 1–20.

43 A. Kaeser, M. Mohankumar, J. Mohanraj, F. Monti, M. Holler, J.-J. Cid, O. Moudam, I. Nierengarten, L. Karmazin-Brelot, C. Duhayon, B. Delavaux-Nicot, N. Armaroli and J.-F. Nierengarten, Heteroleptic Copper(I) Complexes Prepared from Phenanthroline and Bis-Phosphine Ligands, *Inorg. Chem.*, 2013, **52**, 12140–12151.

44 R. Muliadi, S. Suminar, P. Alfian and N. Indah, The UV-visible, Infrared Spectra and Luminescence Analysis of Lanthanum (III) and Neodymium (III)-(Diphenylamino) 3-(2, 2-Bipyridyl) Complexes, *Int. J. Appl. Eng. Res*, 2018, **13**, 4049–4052.

45 S. N. Misra and S. O. Sommerer, Absorption Spectra of Lanthanide Complexes in Solution, *Appl. Spectrosc. Rev.*, 1991, **26**, 151–202.

46 A. Morais, J. P. C. Alves, F. A. S. Lima, M. Lira-Cantu and A. F. Nogueira, Enhanced photovoltaic performance of inverted hybrid bulk-heterojunction solar cells using TiO 2/reduced graphene oxide films as electron transport layers, *J. Photonics Energy*, 2015, **5**, 057408.

47 A. V. Ramya, R. Thomas and M. Balachandran, Mesoporous onion-like carbon nanostructures from natural oil for high-performance supercapacitor and electrochemical sensing applications: Insights into the post-synthesis sonochemical treatment on the electrochemical performance, *Ultrason. Sonochem.*, 2021, **79**, 105767.

48 M. Ge, X. Li, M. Zhang and Z. Liu, Enhanced Photocatalytic Degradation Performance of Antibiotics Using Magadiite-Supported Carbon Nitride Under Visible Light Irradiation, *J. Inorg. Organomet. Polym. Mater.*, 2022, **32**, 678–686.

49 J. M. Stillahn, K. J. Trevino and E. R. Fisher, Deposition of Amorphous CN x Materials in BrCN Plasmas: Exploring Adhesion Behavior as an Indicator of Film Properties, *ACS Appl. Mater. Interfaces*, 2011, **3**, 1402–1410.

50 A. Artemenko, A. Shchukarev, P. Štenclová, T. Wågberg, J. Segervald, X. Jia and A. Kromka, Reference XPS spectra of amino acids, *IOP Conf. Ser. Mater. Sci. Eng.*, 2021, **1050**, 012001.

51 J. Y. Lee, N. Y. Kim, D. Y. Shin, H.-Y. Park, S.-S. Lee, S. Joon Kwon, D.-H. Lim, K. W. Bong, J. G. Son and J. Y. Kim, Nitrogen-doped graphene-wrapped iron nanofragments for high-performance oxygen reduction electrocatalysts, *J. Nanoparticle Res.*, 2017, **19**, 98.

52 Z. Wang, R. Lin, Y. Huo, H. Li and L. Wang, Formation, Detection, and Function of Oxygen Vacancy in Metal Oxides for Solar Energy Conversion, *Adv. Funct. Mater.*, 2022, **32**(7), 2109503.

53 H. S. Casalongue, S. Kaya, V. Viswanathan, D. J. Miller, D. Friebel, H. A. Hansen, J. K. Nørskov, A. Nilsson and H. Ogasawara, Direct observation of the oxygenated species during oxygen reduction on a platinum fuel cell cathode, *Nat. Commun.*, 2013, **4**, 2817.

54 Z. Chen, Z. Tian, L. Zheng, K. Ming, X. Ren, J. Wang and B. Li, (Ho0.25Lu0.25Yb0.25Eu0.25)2SiO5 high-entropy ceramic with low thermal conductivity, tunable thermal expansion coefficient, and excellent resistance to CMAS corrosion, *J. Adv. Ceram.*, 2022, **11**, 1279–1293.

55 N. A. Althumairi, I. Baig, T. S. Kayed, A. Mekki, A. Lusson, V. Sallet, A. Majid, S. Akhtar and A. Fouzri, Structural, morphological, optical, and electrical studies of Tb-doped ZnO micropods elaborated by chemical bath deposition on a p-Si substrate, *Appl. Phys. A*, 2022, **128**, 559.

56 L. Zhang, D. Hu, X. Li, Z. Liu, C. Hu, L. Wu, T. Li, D. Hreniak and J. Li, Effect of Y substitution on the microstructure, magneto-optical, and thermal properties of $(Tb_{1-x}Y_x)$ 3 Al 5 O 12 transparent ceramics, *J. Adv. Ceram.*, 2024, **13**, 529–538.

57 J.-C. G. Bünzli, Chapter 287-Lanthanide Luminescence: From a Mystery to Rationalization, Understanding, and Applications, *Handbook on the Physics and Chemistry of Rare Earths*, 2016, vol. 50, pp. 141–176.

58 S.-N. Zhao, G. Wang, D. Poelman and P. Voort, Luminescent Lanthanide MOFs: A Unique Platform for Chemical Sensing, *Materials*, 2018, **11**, 572.

59 B. Alpha, R. Ballardini, V. Balzani, J. Lehn, S. Perathoner and N. Sabbatini, Antenna effect in luminescent lanthanide cryptates: a photophysical study, *Photochem. Photobiol.*, 1990, **52**, 299–306.

60 M.-J. Tang, Z.-H. Zhu, Y.-L. Li, W.-W. Qin, F.-P. Liang, H.-L. Wang and H.-H. Zou, Specific smart sensing of electron-rich antibiotics or histidine improves the antenna effect, luminescence, and photodynamic sterilization capabilities of lanthanide polyoxometalates, *J. Colloid Interface Sci.*, 2025, **680**, 235–246.

61 M. J. Beltrán-Leiva, E. Solis-Céspedes and D. Páez-Hernández, The role of the excited state dynamic of the antenna ligand in the lanthanide sensitization mechanism, *Dalton Trans.*, 2020, **49**, 7444–7450.

62 D. Genovese, M. Cingolani, E. Rampazzo, L. Prodi and N. Zaccheroni, Static quenching upon adduct formation: a treatment without shortcuts and approximations, *Chem. Soc. Rev.*, 2021, **50**, 8414–8427.

63 R. Siegel and S. Glazier, TNT Sensor: Stern–Volmer Analysis of Luminescence Quenching of Ruthenium Bipyridine, *J. Chem. Educ.*, 2021, **98**, 2643–2648.

64 M.-L. Hu, M. Joharian, S. A. A. Razavi, A. Morsali, D.-Z. Wu, A. Azhdari Tehrani, J. Wang, P. C. Junk and Z.-F. Guo, Phenolic nitroaromatics detection by fluorinated metal-organic frameworks: Barrier elimination for selective sensing of specific group of nitroaromatics, *J. Hazard. Mater.*, 2021, **406**, 124501.

65 S. Liao, Z. Ding, S. Wang, F. Tan, Y. Ge, Y. Cui, N. Tan and H. Wang, Fluorescent nitrogen-doped carbon dots for high selective detecting p-nitrophenol through FRET mechanism, *Spectrochim. Acta, Part A*, 2021, **259**, 119897.

66 A. S. Tanwar, R. Parui, R. Garai, M. A. Chanu and P. K. Iyer, Dual "Static and Dynamic" Fluorescence Quenching Mechanisms Based Detection of TNT *via* a Cationic Conjugated Polymer, *ACS Meas. Sci. Au*, 2022, **2**, 23–30.

67 A. S. Miranda, P. M. Marcos, J. R. Ascenso, M. N. Berberan-Santos, P. J. Cragg, R. Schurhammer and C. Gourlaouen, Critical Analysis of Association Constants between Calixarenes and Nitroaromatic Compounds Obtained by Fluorescence. Implications for Explosives Sensing, *Molecules*, 2023, **28**, 3052.

68 H. R. Khavasi and B. Mir Mohammad Sadegh, Influence of N-heteroaromatic π–π stacking on supramolecular assembly and coordination geometry; effect of a single-atom change in the ligand, *Dalton Trans.*, 2015, **44**, 5488–5502.

69 J. Reedijk, Coordination chemistry beyond Werner: interplay between hydrogen bonding and coordination, *Chem. Soc. Rev.*, 2013, **42**, 1776–1783.

70 X.-L. Sun, B.-X. Shen, S.-Q. Zang and C.-X. Du, Effect of lanthanide contraction on crystal structures of Ln(iii) coordination polymers with dinuclear SBUs based on 3-(4-hydroxypyridinium-1-yl) phthalic acid and oxalic acid, *CrystEngComm*, 2013, **15**, 5910.

71 S.-L. Cai, K. Zhang, S. Wang, Z.-N. Wang, M.-X. Feng, L.-B. Li, J. Fan, S.-R. Zheng and W.-G. Zhang, Lanthanide contraction effect on the crystal structures of 2D lanthanide coordination polymers based on 2-(trifluoromethyl)-1H-imidazole-4,5-dicarboxylic acid, *Struct. Chem.*, 2017, **28**, 577–586.